Comparison of rain fractions over tropical and sub-tropical ocean obtained from precipitation retrieval algorithms for microwave sounders

Satoshi Kida,[1,2] Shoichi Shige,[2] and Takeshi Manabe[1]

Received 30 March 2010; revised 21 July 2010; accepted 1 September 2010; published 17 December 2010.

[1] We compare the fractional occurrence of precipitation (rain fraction) over ocean derived using the Global Satellite Mapping of Precipitation algorithm for the Advanced Microwave Sounding Unit (GSMaP_AMSU) and the Microwave Surface and Precipitation Products System Day 2 rainfall algorithm (NOAA_AMSU) for the Kwajalein radar site and over tropical and subtropical ocean. The rain fractions of GSMaP_AMSU and NOAA_AMSU are lower than that of Kwajalein radar estimates because of failure to detect areas of light rain. Over tropical and subtropical ocean, the rain fraction of GSMaP_AMSU is closer to that obtained using a microwave imager (MWI) and little different from that of Tropical Rainfall Measuring Mission Precipitation Radar (PR) data, whilethe rain fraction of NOAA_AMSU is much smaller than that obtained using MWI or PR data. In the case of the edge of the South Pacific Convergence Zone where the PR observes scattered shallow rain, while NOAA_AMSU fails to detect the scattered rain, GSMaP_AMSU detects the scattered rain through consideration of the scattering index, which is the difference in brightness temperature (Tb) between 89 and 150 GHz. Although the scattering index is designed on the basis that Tb decreases in response to scattering by precipitation at these frequencies and increases rapidly with frequency, there are emission and scattering regimes. Furthermore, the scattering index also responds to emission in light rain with a low concentration of cloud liquid water. As a result, the light rain pixel can be detected using the scattering index to take advantage of the emission signature from raindrops.

Citation: Kida, S., S. Shige, and T. Manabe (2010), Comparison of rain fractions over tropical and sub-tropical ocean obtained from precipitation retrieval algorithms for microwave sounders, *J. Geophys. Res.*, *115*, D24101, doi:10.1029/2010JD014279.

1. Introduction

[2] Accurate observation of the global distribution of precipitation has long been a major scientific goal. Global rainfall maps with high spatial and temporal precision are required not only for scientific research but also for hydrologic applications, agricultural management, and weather forecasts. In spite of its importance, estimation of precipitation with sufficient accuracy and resolution on a global basis is difficult because of the great variability of precipitation in space and time. One of the best approaches to capture global precipitation is to use data from passive microwave radiometers (MWRs) aboard low Earth-orbiting (LEO) satellites and data from infrared radiometers (IRs) aboard geostationary satellites. Data from MWRs have a strong physical relationship with hydrometeors that result in surface precipitation, but an individual LEO satellite provides very sparse sampling of the time-space occurrence of precipitation. On the other hand, data from IRs have high temporal and spatial resolution, but have a weaker relationship with surface precipitation than the data from MWRs because IR channels measure cloud-top temperature, which does not always correlate well with rainfall.

[3] High-precision and high-temporal global rainfall maps are produced by combining data from IRs and MWRs to take advantage of the strengths of each. In producing global rainfall maps, the data from IRs are mainly used to fill the gaps in the estimations of precipitation from MWR data because the estimations of precipitation by IRs are poor. There are two main types of techniques to combine data from IRs and MWRs. One involves the manipulation of IR data in a statistical fashion to mimic the behavior of MWR-derived precipitation estimates (e.g., Tropical Rainfall Measuring Mission (TRMM) Multisatellite Precipitation Analysis (TMPA), *Huffman et al.*, 2007). This technique produces microwave-calibrated IR estimates that match the microwave-based fractional precipitation coverage. The other technique is to use precipitation estimates derived from MWR observations exclusively and transport their features using spatial propagation information obtained from IR data during periods

[1]Department of Aerospace Engineering, Osaka Prefecture University, Sakai, Japan.
[2]Graduate School of Science, Kyoto University, Kyoto, Japan.

0148-0227/10/2010JD014279

when instantaneous MWR data are not available at a location (e.g., Climate Precipitation Center Morphing Technique, CMORPH, *Joyce et al.*, 2004; Global Satellite Mapping of Precipitation Moving Vector with the Kalman Filter method, GSMaP_MVK, *Ushio et al.*, 2009). In both techniques, the fractional occurrence of precipitation obtained from the global precipitation maps depends on the fractional occurrence of precipitation obtained from MWRs. Therefore, the accuracy of rain detection by the precipitation retrieval algorithm for MWRs is important in producing accurate global rainfall maps.

[4] Passive MWRs aboard LEO satellites generally consist of two types: imagers and sounders. Microwave imagers (MWIs) such as the TRMM Microwave Imager (TMI) [*Kummerow et al.*, 1998], the Advanced Microwave Scanning Radiometer for the Earth Observation System (AMSR-E) aboard the Aqua satellite [*Kawanishi et al.*, 2003], and the Special Sensor Microwave Imager (SSM/I) [*Hollinger et al.*, 1990; *Colton and Poe*, 1999] of the Defense Meteorological Satellite Program (DMSP) have channels suitable for observing precipitation such as those at 10 and 19 GHz, which are suitable for observing the emission signal from raindrops, and those at 37 and 85 GHz, which are suitable for observing the scattering signal from ice aloft. On the other hand, microwave sounders (MWSs) such as the Advanced Microwave Sounding Unit (AMSU) aboard the National Oceanic and Atmospheric Administration (NOAA) satellites [*Saunders et al.*, 1995; *Mo*, 1996] are primarily developed for profiling atmospheric temperature and moisture using opaque spectral regions. To optimize the sensor performance, 20 channels are divided among three separate total-power radiometers: AMSU-A1, AMSU-A2, and AMSU-B (NOAA-18 replaced AMSU-B with the similar Microwave Humidity Sounder). AMSU-A has window channels at 23.8, 31.4, 50.3, and 89 GHz and the 50–60 GHz oxygen band. AMSU-B has window channels at 89 and 150 GHz and around the 183 GHz water vapor line. The window channels at 23.8, 31.4, 50.3, 89, and 150 GHz are used to retrieve several important parameters related to the hydrological cycle, and they expand the AMSU capability beyond that of temperature and moisture profiling. Recently, a new type of MWR suitable for precipitation retrieval and temperature and moisture sounding, such as the Special Sensor Microwave Imager-Sounder (SSMIS) [*Kunkee et al.*, 2008], has been carried by satellites.

[5] Three precipitation retrieval algorithms for MWSs have been developed. One is the Microwave Surface and Precipitation Products System (MSPPS) Day 2 algorithm for AMSU (hereinafter referred to as NOAA_AMSU), which was developed at NOAA [*Ferraro et al.*, 2005]. Several researchers found that rainfall derived using early versions of the precipitation retrieval algorithm for the AMSU-B channels differs in many respects from rainfall derived using MWI estimation techniques. The AMSU-B algorithm detects solid hydrometeors, but not liquid. The MWIs similarly sense only solid hydrometeors over land, thus the AMSU-B estimates are roughly comparable for land areas. On the other hand, over ocean, the MWIs sense not only solid hydrometeor but also liquid. As a result, over ocean, the AMSU-B retrievals are less accurate due their inability to detect warm rain from clouds that lack the ice phase, which accounts for 31% of the total rain amount and 72% of the total rain area in the tropics [*Lau and Wu*, 2003]. Thus, the MWS retrievals over ocean are not considered to be included in the baseline Global Precipitation Measurement (GPM) sampling [*Hou et al.*, 2008]. The latest version of NOAA_AMSU has been improved using the emission signals from cloud liquid water (CLW) in AMSU-A channels to retrieve rain that has little or no ice aloft [*Vila et al.*, 2007]. The second is a neural network-based algorithm developed at the Massachusetts Institute of Technology (Cambridge, MA, USA; hereinafter referred to as MIT_AMSU) [*Surussavadee and Staelin*, 2008a, 2008b]. The algorithm is trained using a cloud-resolving model. The third is the Global Satellite Mapping of Precipitation (GSMaP) algorithm for AMSU (hereinafter referred to as GSMaP_AMSU) [*Shige et al.*, 2009], which is based on the GSMaP algorithm for MWIs. The data set of NOAA_AMSU is generated operationally and is available on the Cooperative Institute for Climate Studies (CICS) server (http://cics.umd.edu/~lcao/datasets.html).

[6] While TMPA and CMORPH use precipitation estimates derived from MWS data based on the NOAA_AMSU algorithm in addition to those derived from MWI data, the current GSMaP_MVK uses only precipitation estimates derived from MWI data. Offline tests showed that GSMaP_MVK is more effective when taking rain estimates derived from MWS data using the NOAA_AMSU algorithm in addition to those derived from MWI data using the GSMaP algorithm [*Kubota et al.*, 2009]. It is planned to use rain estimates derived from MWS data using the GSMaP algorithm. Thus, in this study, we compare the fractional occurrences of precipitation over ocean estimated by GSMaP_AMSU and NOAA_AMSU algorithms. The data set of MIT_AMSU is not included in this study because data sets of MIT_AMSU have not been obtained at this point. We also evaluate the fractional occurrences of precipitation using ground validation (GV) radar data, the rain estimates from other microwave imagers, and TRMM Precipitation Radar (PR) [*Kozu et al.*, 2001; *Okamoto and Shige*, 2008].

2. Data

2.1. Microwave Imager

[7] For comparison with the precipitation retrieval algorithms for MWSs, we use the rain product retrieved by the GSMaP algorithm for the TMI (hereinafter this algorithm is referred to as GSMaP_TMI). The basic idea of the GSMaP algorithm is to find the optimal rainfall that gives the radiative transfer model (RTM) FOV-averaged Tb values that fit best the observed Tb values [*Aonashi et al.*, 2009; *Kubota et al.*, 2007]. The GSMaP algorithm consists of a forward calculation part to calculate lookup tables (LUTs), which give the relationship between the rainfall rate and Tb, via a radiative transfer model (RTM), and a retrieval part to estimate precipitation rates from the observed Tb values using the LUTs. In the forward calculation part, LUTs are produced using the four-stream RTM developed by *Liu* [1998]. Atmospheric variables (freezing height, temperature, relative humidity, surface wind, and surface temperature) provided by the Japan Meteorological Agency Global Analysis (GANAL) in a 5 × 5-degree latitude-longitude box are used as input into the RTM. The retrieval calculation

part consists of a rain/no-rain classification (RNC) and an estimation of the rain rates over the delineated rainfall area.

[8] In the RNC over ocean for GSMaP, Tb in the 37 GHz channel with vertical polarization (Tb37v) is used to detect scattered shallow rain at midlatitude [*Kida et al.*, 2009] because Tb in the 37 GHz channel with horizontal polarization (Tb37h) is more sensitive to the surface wind speed, and its use results in the misclassification of rainy areas in the region where the local wind speed is higher than the averaged wind speed of GANAL. However, early work for this study showed that the RNC method using Tb37v misses some shallow rain in the tropics because the sensitivity of Tb37v to light rain is lower than that of Tb37h. Thus, we use not only Tb37v but also the normalized polarization difference [*Petty*, 1994] at 37 GHz (P37), which is a combination of Tb37v and Tb37h for the RNC. Because of the high sensitivity of Tb37h to the surface wind speed, the RNC method over ocean is selected from Tb37v and P37 according to the surface wind speed. P37 is used in the region where the difference in wind speed of GANAL between a 1.25 × 1.25-degree latitude-longitude box and a 5 × 5-degree latitude-longitude box is within 2.0 m s^{-1}, while Tb37v is used in the other region.

[9] GSMaP_TMI arbitrarily assumed a cloud layer with a CLW path of 0.5 kg m^{-2} and relative humidity of 100% below the freezing level [*Aonashi and Liu*, 2000] because the distinction between precipitation and cloud and its relationship with the CLW path is not entirely understood [*Stephens and Kummerow*, 2007]. However, this assumption may be unrealistic for the region where shallow rain is predominant because the CLW path depends on the CLW content (kg m^{-3}) and cloud depth. Therefore, over the region where shallow rain is predominant, the parameterization of the CLW path as a function of storm height [*Kida et al.*, 2009] is applied:

$$CLW = 0.1 \times SH \tag{1}$$

where SH (km) is the storm height derived from the PR standard product 3A25, which is a monthly composite of TRMM PR data with gridded 5 degree spatial resolution. We also parameterize the relative humidity, which was assumed to be 100% below the freezing level. The relative humidity is 100% under the SH and values from GANAL above the SH. In this study, the parameterization is applied to GSMaP_TMI.

[10] We also used the current (version 6) level 2 standard products of the TRMM TMI published by the National Aeronautics and Space Administration (NASA) and the Japan Aerospace Exploration Agency (JAXA). The level 2 standard product 2A12 is the rain estimation of the TMI produced by the Goddard PROFiling (GPROF) algorithm (hereinafter referred to as GPROF_TMI) [*Kummerow et al.*, 2001; *Olson et al.*, 2006]. The basis of GPROF_TMI is a Bayesian framework in which retrieved precipitation is constructed from cloud-resolving, model-generated profiles that are radiatively consistent with observations.

2.2. Microwave Sounder

[11] We compare the fractional occurrences of precipitation estimated by two precipitation algorithms for MWSs over ocean: the Microwave Surface and Precipitation Products System (MSPPS) Day 2 rainfall algorithm (NOAA_AMSU) [*Weng and Grody*, 2000; *Zhao and Weng*, 2002; *Ferraro et al.*, 2005; *Vila et al.*, 2007] and the Global Satellite Mapping of Precipitation Algorithm (GSMaP_AMSU) [*Shige et al.*, 2009]. Polar-orbiting satellites such as the NOAA satellite collect two samples per day at about the same nominal times, and thus mean estimates inferred from these observations incur an intrinsic diurnal bias. On the other hand, the TRMM, which is in a non-Sun-synchronous orbit, reduces the diurnal bias because of its precession through the diurnal cycle in a period of about 46 days. Therefore, to reduce the diurnal bias incurred by the AMSU observation, we use data from the four AMSU sensors aboard the NOAA satellites (NOAA-15, NOAA-16, NOAA-17, and NOAA-18), which are typically spaced about 4 h in time, thus giving a better representation of the diurnal cycle. The RNC method in each algorithm is briefly described in the following subsections because the fractional occurrences of precipitation are affected by the rain detection.

2.2.1. MSPPS Day 2 Rainfall Algorithm (NOAA_AMSU)

[12] The algorithm originates from the works of *Weng and Grody* [2000] and *Zhao and Weng* [2002]. The ice water path (IWP) and ice particle effective diameter (De) were simultaneously retrieved from Tb at 89 and 150 GHz (hereinafter referred to as Tb89 and Tb150, respectively) through two processes: simplifying the radiative transfer equation into a two-stream approximation and estimating the cloud-base and cloud-top Tb values from AMSU measurements at 23.8 and 31.4 GHz. The rain rate was computed on the basis of an IWP and rain rate relation derived from the GPROF [*Kummerow et al.*, 2001; *Olson et al.*, 2006] algorithm database, which contains the profiles of various hydrometeors generated from cloud-resolving models. The rain rate is computed when the IWP is greater than or equal to 0.05 kg m^{-2} and De is greater than or equal to 0.3 mm if the IWP and De retrievals fall within an acceptable range (between 0 and 3.0 kg m^{-2} and between 0 and 3.5 mm, respectively).

[13] Additionally, because the rain retrieval based on the IWP can estimate only precipitation that is detectable from a scattering signature, the CLW path retrieved from AMSU-A channels and the convective index (CI) calculated using the AMSU-B moisture channels are used as a proxy for retrieving rain that has little or no ice. In detecting shallow rain, NOAA_AMSU uses the CLW path as a proxy for retrieving rain and employs a high CLW path of 0.4 kg m^{-2} as a threshold of RNC to avoid false signatures in moist, nonraining clouds and uncertainty in the AMSU-A CLW calculations [*Vila et al.*, 2007]. The rain rate is computed from the relationship between the rain rates and the CLW path when there is a lack of ice structure (Tb89 < Tb150) and the rain rate derived from the IWP is greater than or equal to 0 mm h^{-1} and the CLW path is greater than the threshold value of 0.4 kg m^{-2}.

2.2.2. GSMaP Algorithm for a Microwave Sounder (GSMaP_AMSU)

[14] GSMaP_AMSU is a precipitation algorithm developed for an MWS and based on the GSMaP algorithm for an MWI [*Shige et al.*, 2009]. Like the GSMaP algorithm for an MWI, GSMaP_AMSU consists of a forward calculation part to calculate LUTs giving the relationship between the rainfall

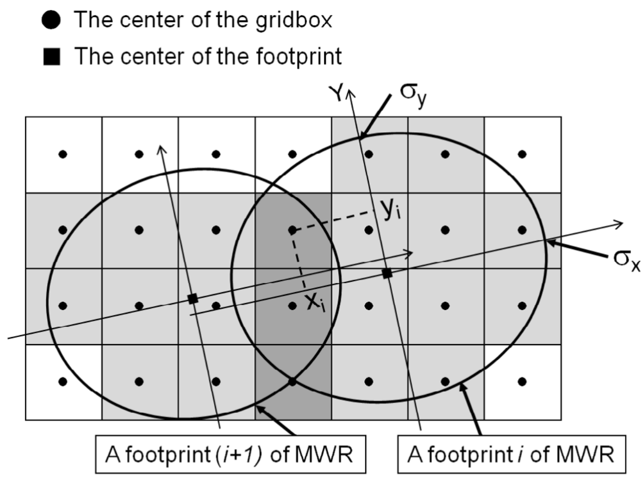

Figure 1. Schematic of the conversion of the rainfall rate from a footprint to a grid.

rate and Tb using a developed RTM and a retrieval part to estimate precipitation rates from the observed Tb values using the LUTs.

[15] In the retrieval part, a rain pixel is classified before the rainfall rate is estimated. The method of RNC over ocean comprises two processes. In the first process, an emission signature at 31 GHz is used to detect warm rain from clouds that lack the ice phase. The condition for the determination of a rainy pixel in the emission-based method is

$$\mathrm{Tb31} > \mathrm{Tb31}_{\mathrm{LUT0}} \tag{2}$$

where $\mathrm{Tb31}_{\mathrm{LUT0}}$ is Tb31 at 0 mm h^{-1} in the LUT. In the second process, an SI is computed from Tb89 and Tb150:

$$\mathrm{SI} = (\mathrm{Tb89} - \mathrm{Tb89}_{\mathrm{LUT0}}) - (\mathrm{Tb150} - \mathrm{Tb150}_{\mathrm{LUT0}}) \tag{3}$$

where $\mathrm{Tb89}_{\mathrm{LUT0}}$ and $\mathrm{Tb150}_{\mathrm{LUT0}}$ are Tb89 and Tb150 at 0 mm h^{-1} in the LUTs, respectively. Because scattering from ice lowers Tb and the Tb reduction is greater at 150 GHz than at 89 GHz, the condition for the determination of a rainy pixel is

$$\mathrm{SI} > 0. \tag{4}$$

[16] A cloud layer with a CLW path of 0.5 kg m^{-2} below the freezing level is arbitrarily assumed by GSMaP_AMSU as well as GSMaP_TMI. In this study, over the region where shallow rain is predominant, the parameterization of the CLW path given by equation (1) is applied to GSMaP_AMSU.

2.3. Satellite-Borne Radar

[17] The current (version 6) level 2 standard product 2A25 [*Iguchi*, 2007; *Iguchi et al.*, 2009] is used for the rain estimation of the PR. The 2A25 algorithm estimates the true effective reflectivity factor Z_e at 13.8 GHz in each radar resolution cell from the vertical profiles of the measured reflectivity factor Z_m. The rainfall rate is then calculated from the estimated Z_e. The PR has a minimum detectable reflectivity of 17 dBZ, which corresponds to approximately 0.7 mm h^{-1} after the TRMM satellite orbit boost on August 2001 [*Shimizu et al.*, 2009]. Before processing the precipitation retrieval, each pixel is classified into one of three rain categories ("rain certain," "rain possible," and "no rain"). The labeling of pixels as rain possible often results from noise, and the current standard product 2A25 does not provide rainfall retrievals for rain possible pixels because of the serious contamination of no rain pixels among rain possible pixels [*Takahashi and Iguchi*, 2008]. Therefore, the 2A25 algorithm underestimates rain coverage.

2.4. Ground-Based Radar

[18] GV data used in this study are the official TRMM 2A53 rain products for Kwajalein (KWAJ) produced by the TRMM Satellite Validation Office and available from the Goddard Earth Sciences (GES) Data and Information Services Center (DISC). The 2A53 product provides the instantaneous rain rate at 2 km × 2 km horizontal resolution, extending 150 km from the respective GV radar. In this study, the GV radar data were processed using the official Version 7 algorithm of the 2A53 product. The algorithm applies the window probability matching method (WPMM) [*Rosenfeld and Wolff*, 1995] to the statistical determination of rain rates from radar reflectivities. The GV processing system and descriptions of the GV algorithms are detailed in *Wolff et al.* [2005]. In the present study, the 2 km data were averaged over 0.1 degree grids for comparison with the satellite estimates.

2.5. Conversion to Gridded Data

[19] To compare the rain estimates at the same resolution, we remapped each rain estimation derived from the MWI and MWS into a 0.1 degree global grid. When the center of a gridbox is included by a single footprint, the gridbox is assigned with the rainfall rate of the footprint. On the other hand, when the center of a gridbox is included by multiple footprints, the rainfall rate within the gridbox is averaged according to the distance from the center of a footprint. The weighted average rainfall rate in a grid is defined by

$$\mathrm{R}_{\mathrm{grid}} = \frac{\sum_{\mathrm{i}} \mathrm{W_i} \times \mathrm{R_i}}{\sum_{\mathrm{i}} \mathrm{W_i}}, \tag{5}$$

in which

$$\mathrm{W_i} = \exp\left(-\ln(2) \times \left\{\left(\frac{\mathrm{x_i}}{\sigma_\mathrm{i}}\right)^2 + \left(\frac{\mathrm{y_i}}{\sigma_\mathrm{i}}\right)^2\right\}\right) \tag{6}$$

where *i* is the number of the footprint and R_i is the rainfall rate of the footprint *i* of the MWRs. A position of (x_i, y_i) indicates a position of the center of the gridbox in a system of coordinates with their origin at the center of the footprint *i*. The MWR footprint takes the form of an ellipse, and the long-axis direction and short-axis direction are defined as the *x*-direction and *y*-direction (Figure 1). We employ a short axis σ_x and long axis σ_y of 3.6 and 2.3 km for the TMI, which are half the footprint dimensions for the 85 GHz channel, which has the smallest footprint of any channel used in the algorithm. The AMSU footprint size varies for each scan angle because the AMSU-B/MHS radiometer employs cross-track scanning to view the Earth. Therefore, we

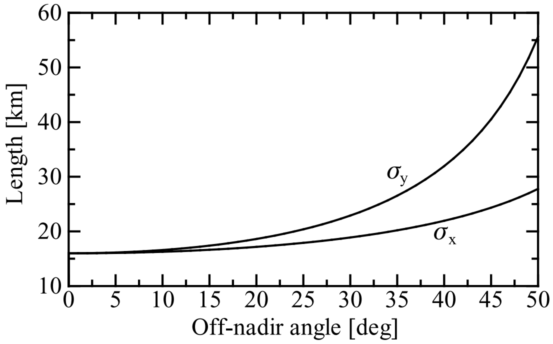

Figure 2. Variation of the lengths of the short axis σ_x and long axis σ_y as functions of the off-nadir angle for AMSU.

employ variable FOVs of 16 km × 16 km at nadir and 52 km × 27 km at limb for the AMSU-B/MHS (Figure 2), from which the precipitation products for MWSs are retrieved.

[20] The 2 km data from the Kwajalein radar and the 5 km data from the PR were simply averaged over a 0.1 degree grid because the resolutions of the Kwajalein radar data and PR data are finer than the 0.1 degree grid.

3. Results

3.1. Comparison With the Rain Fraction Measured at the Kwajalein Radar Site

[21] The rain fraction f is defined by

$$f = \frac{N_{rain}}{N_{all}} \tag{7}$$

where N_{rain} is the number of rain gridboxes and N_{all} is the number of gridboxes observed by the satellite. It is important to note that the rain fraction is sensitive to the spatial scale.

[22] Figure 3 compares the rain fractions of the Kwajalein radar estimates (KR estimates) and the satellite estimates for 2007. For comparison, all satellite estimates and KR estimates were matched in both time and space, which effectively mitigated the temporal sampling errors with respect to the noncontiguous sampling of the satellites as a source of uncertainty. The rain fractions of the KR estimates range from 24.9% to 26.2%. The rain fractions of the satellite estimates are 10.5% for GSMaP_AMSU, 7.6% for NOAA_AMSU, 15.6% for GSMaP_TMI, 15.0% for GPROF_TMI, and 12.9% for the PR. Because the Kwajalein radar, which has finer horizontal resolution (2 km) and higher sensitivity than the satellites, can detect isolated convective rain and a large area of stratiform rain having a low rain rate [*Schumacher and Houze*, 2000], the rain fractions estimated by the satellites are half those of the KR estimates. The rain fractions of GSMaP_AMSU and NOAA_AMSU are lower than the rain fractions of GSMaP_TMI, GPROF_TMI, and the PR. The rain fraction of GSMaP_AMSU is greater than that of NOAA_AMSU, indicating that GSMaP_AMSU detects a larger rain area than NOAA_AMSU.

[23] Figure 4 shows the rain fractions as cumulative fractions, being functions of the rain rate. The rain fractions of GSMaP_AMSU, NOAA_AMSU, and the PR are small for a rain rate lower than 0.1 mm h^{-1}. This indicates that GSMaP_AMSU, NOAA_AMSU, and the PR fail to detect an area of light rain with a rain rate less than 0.1 mm h^{-1}. In the case of NOAA_AMSU, a very small rain fraction for rain rates less than 1.0 mm h^{-1} and a rapid increase in the rain fraction around 1.0 mm h^{-1} are found. The rain fraction of GSMaP_AMSU increases continuously in the same way as the rain fractions of other estimates for a rain rate greater than 0.1 mm h^{-1}.

[24] Table 1 shows the cumulative rain fractions between 0.0 and 1.0 mm h^{-1} and between 1.0 and 10.0 mm h^{-1}. The rain fraction of MWSs between 0.0 and 1.0 mm h^{-1} are lower than those of MWIs and PR. On the other hand, the rain fraction of MWSs between 1.0 and 10.0 mm h^{-1}

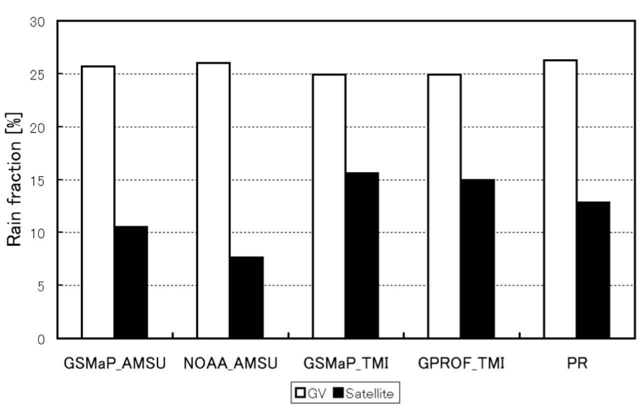

Figure 3. Satellite estimate versus Kwajalein radar estimate of the rainfall fraction in 2007.

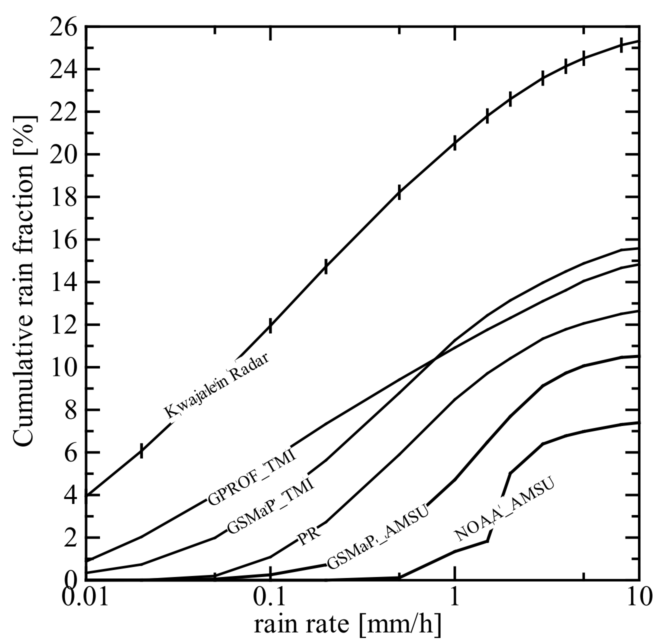

Figure 4. Cumulative rain fractions as functions of the rain rate for Kwajalein radar, GSMaP_AMSU, NOAA_AMSU, GSMaP_TMI, GPROF_TMI, and the PR.

Table 1. Cumulative Rain Fractions Between 0.0 and 1.0 mm h^{-1} and Between 1.0 and 10.0 mm h^{-1}

	0 ~ 1 mm h^{-1}	1 ~ 10 mm h^{-1}
GSMaP_AMSU	4.72	5.80
NOAA_AMSU	1.34	6.05
GSMaP_TMI	11.3	4.32
GPROF_TMI	10.9	3.91
PR	8.49	4.16

are slightly higher than those of MWIs and PR. This indicates that the rain detection of MWSs is almost comparable to those of MWIs and PR for a moderate rain rate.

3.2. Tropical and Subtropical Ocean

[25] Figure 5 shows the rain fractions of GSMaP_AMSU, NOAA_AMSU, GSMaP_TMI, GPROF_TMI, and the PR for a 2 degree longitude-latitude box. In the Intertropical Convergence Zone (ITCZ) and South Pacific Convergence Zone (SPCZ), where there are generally large rain amounts, high rain fractions (~10%) for all MWRs are found. On the other hand, in subtropical oceans, where the mean descending branch of the meridional Hadley cell suppresses the convection of clouds, low rain fractions (~6%) are found. The rain fractions over ocean between 30°S and 30°N are 10.1% for GSMaP_AMSU, 7.2% for NOAA_AMSU, 13.3% for GSMaP_TMI, 13.4% for GPROF_TMI, and 9.3% for the PR. The rain fractions of GSMaP_AMSU are between the rain fractions of the PR and TMI, while the rain fraction of NOAA_AMSU is the smallest. On the other hand, the rain amounts over ocean between 30°S and 30°N are 79.0 mm $month^{-1}$ for GSMaP_AMSU, 82.8 mm $month^{-1}$ for NOAA_AMSU, 82.3 mm $month^{-1}$ for GSMaP_TMI, 80.6 mm $month^{-1}$ for GPROF_TMI, and 77.9 mm $month^{-1}$ for PR. The rain amount of GSMaP_AMSU is lower than those of MWIs, while the rain amount of NOAA_AMSU is higher than those of MWIs. Figure 6 shows the zonal averaged rain fractions of GSMaP_AMSU, NOAA_AMSU, GSMaP_TMI, GPROF_TMI and PR. The rain fractions of all products are at their peak around 7°N. The rain fractions of GSMaP_AMSU and NOAA_AMSU have bias lower than that of MWIs over tropical and subtropical oceans. The comparison between GSMaP_AMSU and PR shows the excellent agreement of the rain fraction from 30°S to 2°N. On the other hand, the rain fraction of GSMaP_AMSU is larger than that of PR in the region between about 2°N and 12°N and lower in the region between about 12°N and

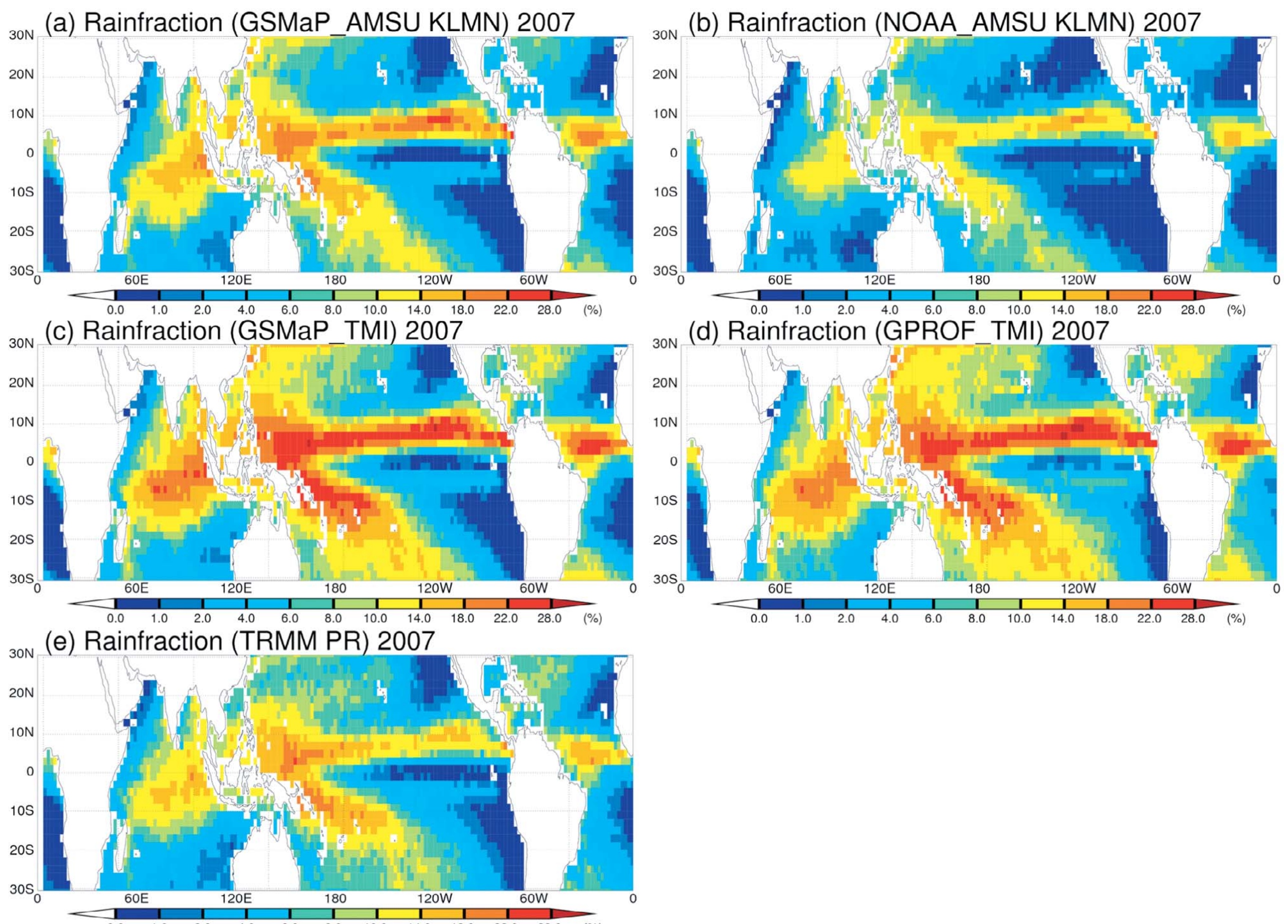

Figure 5. Rain fractions for (a) GSMaP_AMSU, (b) NOAA_AMSU, (c) GSMaP_TMI, (d) GPROF_TMI, and (e) the PR in a 2 degree latitude-longitude box.

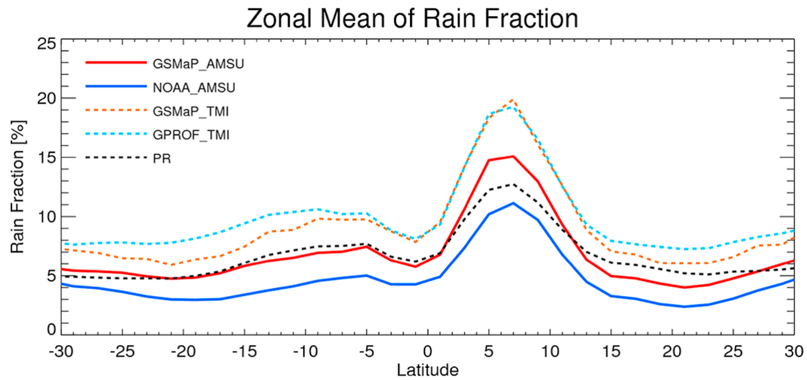

Figure 6. Zonal averaged rain fractions for GSMaP_AMSU, NOAA_AMSU, GSMaP_TMI, GPROF_TMI, and PR.

28°N. Although the global averages for GSMaP_AMSU and PR are similar, regional differences exist. Figures 7a, 7b, 7c, and 7d show differences in the rain fractions between the MWS and MWI. The rain fraction of GSMaP_AMSU is lower than that of the MWI in parts of the ITCZ and SPCZ. On the other hand, the rain fraction of NOAA_AMSU is much lower than that of the MWI over tropical and subtropical ocean. This result is consistent with the result obtained at the Kwajalein radar site (Figure 3). Figures 7e and 7f show the difference in the rain fraction between the MWS and PR. While the rain fraction of GSMaP_AMSU is close to that of the PR over

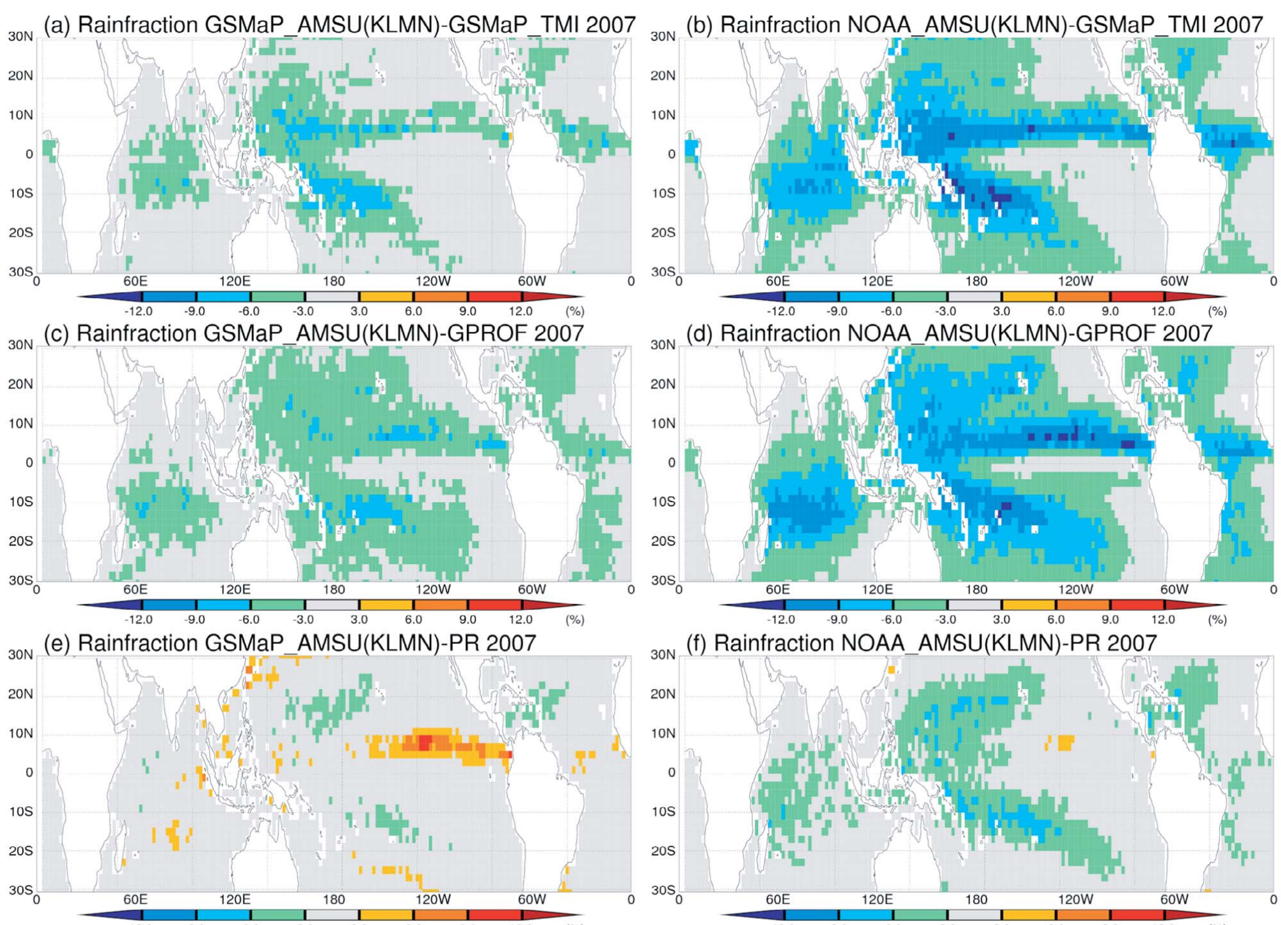

Figure 7. Difference in the rain fraction between (a) GSMaP_AMSU and GSMaP_TMI, (b) NOAA_AMSU and GSMaP_TMI, (c) GSMaP_AMSU and GPROF_TMI, (d) NOAA_AMSU and GPROF_TMI, (e) GSMaP_AMSU and PR, and (f) NOAA_AMSU and the PR.

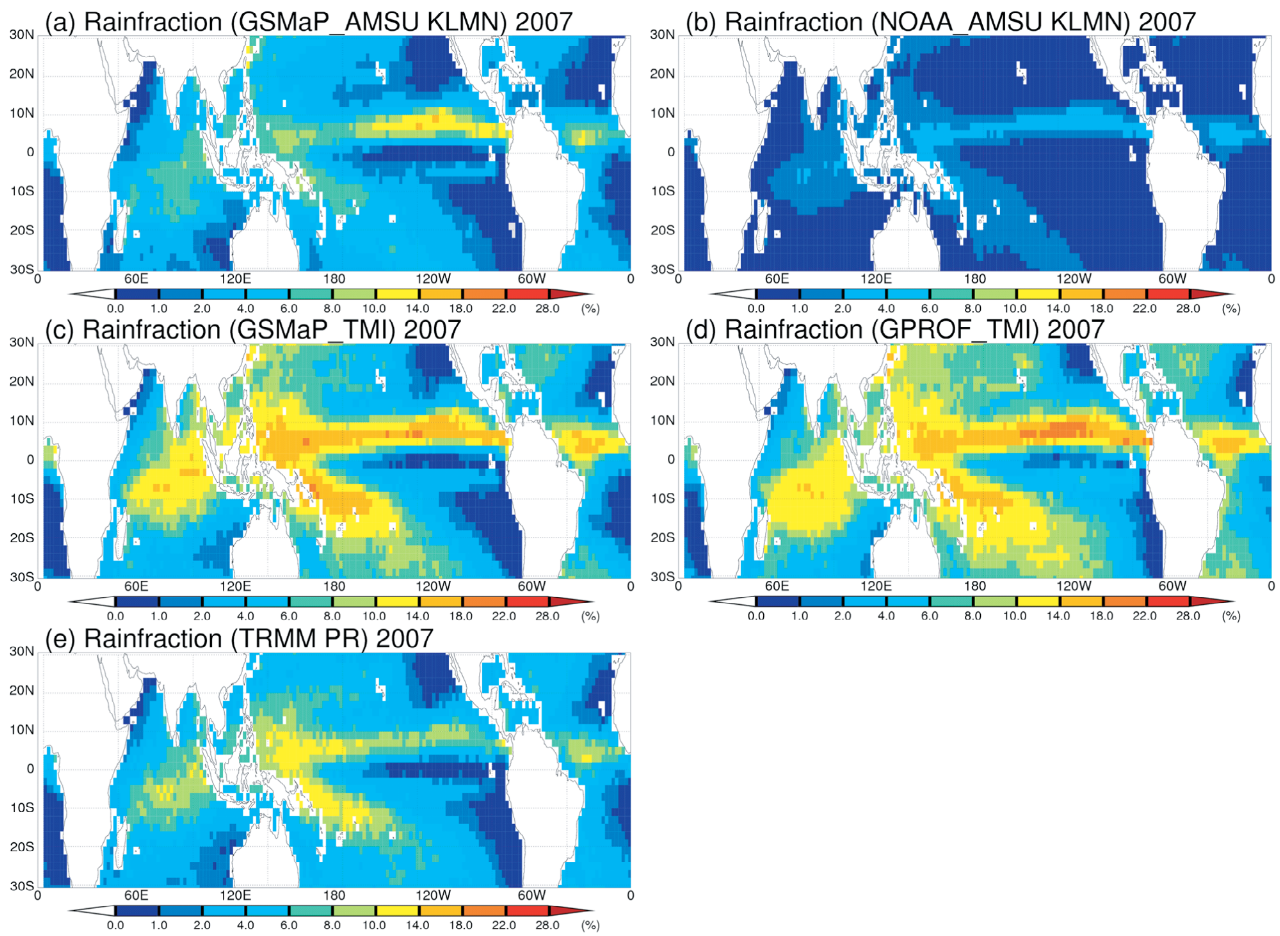

Figure 8. The same as Figure 5 but the rain fractions of the satellite estimates for a rain rate less than 1.0 mm h^{-1}.

the western ITCZ, over the eastern ITCZ, the rain fraction of GSMaP_AMSU is greater than that of the PR. Precipitation systems over the eastern Pacific exhibit a number of significant differences when compared with those over the western Pacific warm pool [*Berg et al.*, 2002]. *Shige et al.* [2008] hypothesized that the PR underestimates the rainfall rate because of the higher concentration of smaller raindrops in clouds over the eastern Pacific than over the western Pacific. The high concentration of small raindrops in clouds over the eastern Pacific may lead to the failure of the PR to detect rain, resulting in the low rain fraction recorded by the PR over the eastern ITCZ. Over subtropical ocean such as the edge of the SPCZ, the rain fraction of NOAA_AMSU is lower than that of the PR, but the rain fraction of GSMaP_AMSU is comparable to that of the PR.

[26] Figure 8 shows the rain fraction of the satellite estimates for a rain rate lower than 1.0 mm h^{-1}. The rain fractions over ocean between 30°S and 30°N are 5.0% for GSMaP_AMSU, 1.3% for NOAA_AMSU, 9.1% for GSMaP_TMI, 9.4% for GPROF_TMI, and 5.8% for the PR. The rain fraction of GSMaP_AMSU is comparable to the rain fraction of the PR and is half the rain fractions of GSMaP_TMI and GPROF_TMI. On the other hand, the rain fraction of NOAA_AMSU is the lowest of all rain fractions and is small (~4%) over tropical and subtropical oceans. This result shows that NOAA_AMSU misses light rain with a rain rate lower than 1.0 mm h^{-1} over tropical and subtropical oceans.

[27] Figure 9 presents the case that the AMSU observations match the PR observation at the edge of the SPCZ (36.2°S–6.2°S, 125.5°W–95.5°W). The time lag between the PR and AMSU is about 470 seconds. In this case, the PR observes scattered rain (Figure 9a). GSMaP_AMSU can detect scattered shallow rain in the middle of the swath (Figure 9b), while NOAA_AMSU misses the scattered shallow rain (Figure 9c). Figure 9d shows the freezing height derived from GANAL on a 1.25-degree grid and the rain top height derived from PR2A25. The rain top observed by the PR is below the freezing height in this case. In this region, because the mean descending branch of the meridional Hadley cell suppresses the convection of clouds, shallow rain is predominant. Figure 9e shows the CLW retrieved from AMSU-A channels. Over the region including the scattered shallow rain, a CLW path of about 0.25 kg m^{-2} is found. To detect shallow rain, NOAA_AMSU uses the CLW path as a proxy for retrieving rain and employs a high-CLW path of 0.4 kg m^{-2} as a threshold value of RNC to avoid false signatures in moist, nonraining clouds and uncertainty in

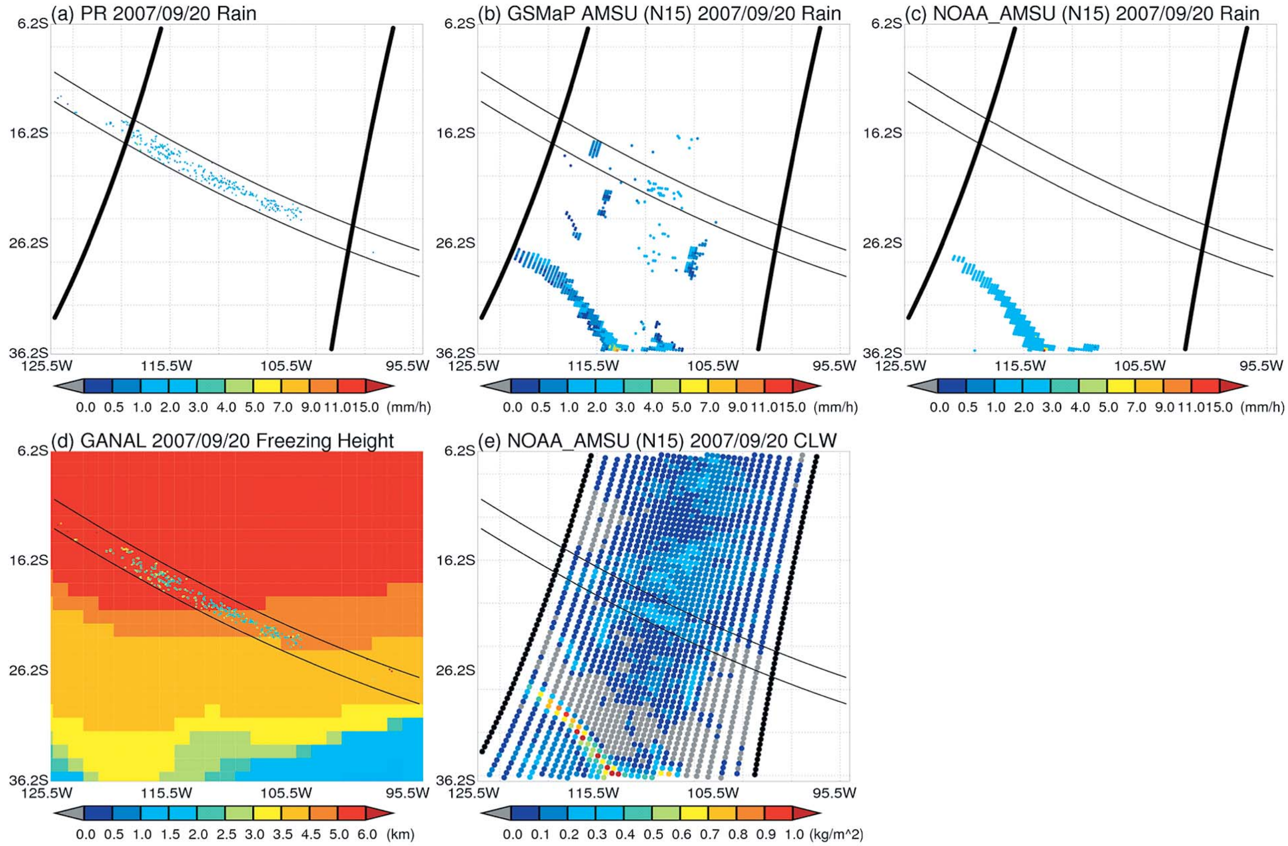

Figure 9. Case in which the AMSU observation matches the PR observation on 20 September 2007 (TRMM orbit number 56103) at the edge of the SPCZ (36.2°S–6.2°S, 125.5°W–95.5°W). Rain derived from (a) PR, (b) GSMaP_AMSU and (c) NOAA_AMSU. (d) Freezing height derived from GANAL in a 1.25 degree grid and rain top height derived from PR. (e) CLW path derived using the NOAA_AMSU. The thick lines are the edge of the AMSU swath, and the thin lines are the edge of the PR swath.

the AMSU-A CLW calculations [*Vila et al.*, 2007]. Therefore, the threshold value of RNC is higher than the CLW path over the region including the scattered shallow rain, which leads to no-rain classification.

[28] Figure 10 shows the result of RNC for GSMaP_AMSU with different RNC threshold values of the CLW path. In GSMaP_AMSU, each footprint is separated into four RNC categories using equations (2) and (4). RN0 is

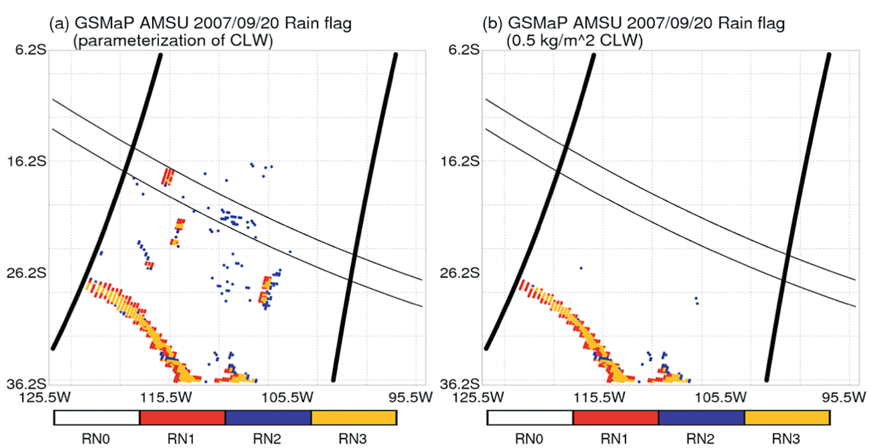

Figure 10. Result of rain classification in GSMaP_AMSU with (a) parameterization of the CLW path as a function of the storm height, which is typically 0.25 kg m^{-2}, and (b) 0.5 kg m^{-2} CLW. RN0 is classified as a no-rain pixel by equations (2) and (4), RN1 is classified as a rain pixel only by equation (2), RN2 is classified as a rain pixel only by equation (4), and RN3 is classified as a rain pixel by equations (2) and (4).

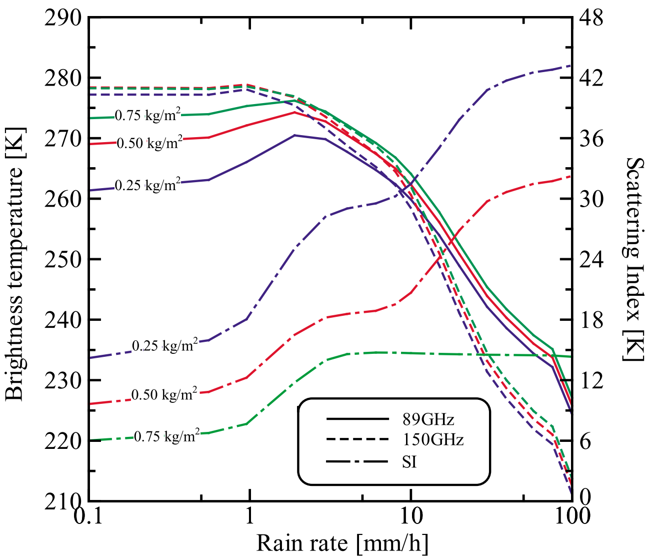

Figure 11. Brightness temperature as a function of the rain rate. The solid line is the brightness temperature at 89 GHz, and the dashed line is the brightness temperature at 150 GHz. The dashed-dotted line shows the SI computed by equation (3). The different colors indicate different RNC threshold values of CLW: blue lines are for 0.25 kg m^{-2}, red lines for 0.50 kg m^{-2}, and green lines for 0.75 kg m^{-2}.

the classification of a no-rain pixel according to equations (2) and (4), RN1 is the classification of a rain pixel according to only equation (2), RN2 is the classification of a rain pixel according to only equation (4), and RN3 is the classification of a rain pixel according to equations (2) and (4). For GSMaP_AMSU with the parameterization of the CLW path as a function of storm height [*Kida et al.*, 2009], which is typically 0.25 kg m^{-2} in this region, the scattered rain is classified as RN2, which is derived only from the SI (Figure 10a). For GSMaP_AMSU with a threshold of 0.5 kg m^{-2} for the RNC, which is used in the original version of GSMaP_AMSU, the scattered shallow rain is classified as no rain (Figure 10b). The emission-based method [equation (2)] that uses the AMSU-A channels fails to detect scattered shallow rain because the scattered shallow rain is less than the resolution of the AMSU-A channels used.

[29] Figure 11 shows the LUT for Tb89 and Tb150 with three different CLW thresholds (0.25, 0.5, and 0.75 kg m^{-2}). Tb89 increases with the rain rate below 2.0 mm h^{-1} because of the emission from the raindrops and is saturated at about 2.0 mm h^{-1}. Here, "diff_Tb89$_{LUT}$" is defined as

$$\mathrm{diff\_Tb89_{LUT}} = \mathrm{Tb89_{LUTsat}} - \mathrm{Tb89_{LUT0}} \tag{8}$$

where Tb89$_{LUTsat}$ is Tb89 at saturation in the LUTs. diff_Tb89$_{LUT}$ is large for the CLW threshold of 0.25 kg m^{-2}, which is found in the shallow rain over subtropical ocean (Figure 9e), and small for 0.75 kg m^{-2} because the emission signature is weaker for 0.25 kg m^{-2} CLW than for 0.75 kg m^{-2} CLW. A larger value of diff_Tb89$_{LUT}$ for 0.25 kg m^{-2} CLW than for 0.75 kg m^{-2} CLW indicates that Tb89 for 0.25 kg m^{-2} CLW represents the rain rate unambiguously because Tb89 for the CLW of 0.25 kg m^{-2} in the LUT increases more rapidly with rainfall. On the other hand, Tb150 varies only slightly for a rain rate less than 2.0 mm h^{-1} and decreases above 2.0 mm h^{-1} because of scattering from ice. Thus, although the SI is designed on the basis that ice scattering lowers Tb and increases rapidly with frequency, there are emission and scattering regimes and the SI also responds to emission in light rain with a low CLW path. As a result, the light rain pixel can be detected using the SI to take advantage of the emission signature from raindrops at 89 GHz.

4. Summary

[30] In this study, we compare the fractional occurrence of precipitation (rain fraction) obtained using two microwave precipitation algorithms for MWSs.

[31] At the Kwajalein radar site, the rain fractions of satellite-based estimates are not even half the rain fractions of Kwajalein radar estimates (KR estimates) because the KR, which has finer horizontal resolution and higher sensitivity, can detect isolated convective rain and a large area of stratiform rain with a low rain rate. The rain fractions of GSMaP_AMSU and NOAA_AMSU are lower than the rain fractions of MWI algorithms (GSMaP_TMI and GPROF_TMI) and the PR. Small rain fractions of GSMaP_AMSU, NOAA_AMSU, and the PR result from the failure to detect the light rain area with a rain rate less than 0.1 mm h^{-1}. For NOAA_AMSU, there is a very small rain fraction for rain rates less than 1.0 mm h^{-1} and a rapid increase in the rain fraction around 1.0 mm h^{-1}. The rain fraction of GSMaP_AMSU increases continuously in the same way as the rain fractions of other estimates for a rain rate greater than 0.1 mm h^{-1}.

[32] In the comparison of the rain fractions between the MWS and MWI over tropical and subtropical oceans, the rain fractions of GSMaP_AMSU and NOAA_AMSU have bias lower than that of MWIs over tropical and subtropical oceans. The rain fraction of GSMaP_AMSU is lower than that of the MWI in parts of the ITCZ and SPCZ. On the other hand, the rain fraction of NOAA_AMSU is much lower than that of the MWI over tropical and subtropical ocean. The rain fraction is lower for NOAA_AMSU than for GSMaP_AMSU because NOAA_AMSU fails to detect the large rain area with a rate less than 1.0 mm h^{-1}. In the comparison of the rain fractions between the MWS and PR, although the global averages for GSMaP_AMSU and PR are similar, the rain fraction of GSMaP_AMSU is larger than that of the PR in the eastern ITCZ, possibly because the PR algorithm fails to detect the rain owing to the higher concentration of smaller raindrops in clouds over the eastern Pacific. On the other hand, over subtropical ocean such as the edge of the SPCZ, the rain fraction of NOAA_AMSU is lower than that of the PR.

[33] In the case of the edge of the SPCZ, where the PR observes scattered shallow rain, while NOAA_AMSU fails to detect the scattered rain, GSMaP_AMSU detects some of the scattered rain. For light rain, Tb89 increases with the rain rate below 2.0 mm h^{-1} because of the emission from the cloud and raindrops and is saturated at about 2.0 mm h^{-1}. A larger diff_Tb89$_{LUT}$ for 0.25 kg m^{-2} CLW than for

0.75 kg m^{-2} CLW indicates that Tb89 for 0.25 kg m^{-2} CLW represents the rain rate unambiguously. Therefore, although the SI is designed on the basis that Tb decreases in response to scattering by precipitation at these frequencies and increases strongly with frequency, there are emission and scattering regimes and the SI also responds to emission in light rain with a low CLW path. As a result, the light rain pixel can be detected using the SI to take advantage of the emission signature from raindrops. Therefore, it is suggested that the MWS retrievals over ocean are incorporated into high spatial and temporal resolution precipitation products, although the MWS retrievals over ocean are not considered to be included in the baseline GPM sampling [*Hou et al.*, 2008].

[34] In this study, we compare the rain fractions over tropical and subtropical ocean. On the other hand, the rain fractions outside tropical and subtropical ocean have not been compared. However, in the future, there will be more opportunities to make observation of higher latitudes from satellite in the GPM Mission [*Smith et al.*, 2007], so the rain fraction at higher latitudes is important. Thus, we will compare the rain fractions outside tropical and subtropical ocean in future work.

[35] **Acknowledgments.** This study is supported by the Mitsui & Co., Ltd., Environment Fund and by the Japan Aerospace Exploration Agency/Earth Observation Research Center (JAXA/EORC) TRMM project. The authors thank Professor K. Okamoto (Tottori University of Environmental Studies) for valuable comments. The authors also thank Dr. G. Liu for providing the RTM code.

References

Aonashi, K., and G. Liu (2000), Passive microwave precipitation retrievals using TMI during the Baiu period of 1998. Part I: Algorithm description and validation, *J. Appl. Meteor.*, *39*(12), 2024–2037.
Aonashi, K., et al. (2009), GSMaP passive microwave precipitation retrieval algorithm: Algorithm description and validation, *J. Meteorol. Soc. Japan*, *87A*, 119–136.
Berg, W., C. Kummerow, and C. A. Morales (2002), Differences between East and West Pacific rainfall systems, *J. Clim.*, *15*(24), 3659–3672.
Colton, M. C., and G. A. Poe (1999), Intersensor calibration of DMSP SSM/I's: F-8 to F-14, 1987–1997, *IEEE Trans. Geosci. Remote Sens.*, *37*(1), 418–439.
Ferraro, R., F. Weng, N. Grody, L. Zhao, H. Meng, C. Kongoli, P. Pellegrino, S. Qiu, and C. Dean (2005), NOAA operational hydrological products derived from the advanced microwave sounding unit, *IEEE Trans. Geosci. Remote Sens.*, *43*(5), 1036–1049.
Hollinger, J. P., J. L. Peirce, and G. A. Poe (1990), SSM/I instrument evaluation, *IEEE Trans. Geosci. Remote Sens.*, *28*(5), 781–790.
Hou, A. Y., G. Skofronick-Jackson, C. D. Kummerow, and J. M. Shepherd (2008), Global precipitation measurement, in *Precipitation: Advances in Measurement, Estimation, and Prediction*, edited by S. Michaelides, pp. 131–169, Springer, New York.
Huffman, G., R. Adler, D. Bolvin, G. Gu, E. Nelkin, K. Bowman, Y. Hong, E. Stocker, and D. Wolff (2007), The TRMM Multisatellite Precipitation Analysis (TMPA): Quasi-global, multiyear, combined-sensor precipitation estimates at fine scales, *J. Hydrometeorol.*, *8*(1), 38–55.
Iguchi, T. (2007), Space-borne radar algorithms, in *Measuring Precipitation From Space-EURAINSAT and the Future*, edited by V. Levizzani, P. Bauer, and F. J. Turk, pp. 199–212, Springer, New York.
Iguchi, T., T. Kozu, J. Kwiatkowski, R. Meneghini, J. Awaka, and K. Okamoto (2009), Theoretical basis of the evolution of the TRMM rain profiling algorithm, *J. Meteorol. Soc. Japan*, *87A*, 1–30.
Joyce, R. J., J. E. Janowiak, P. A. Arkin, and P. Xie (2004), CMORPH: A method that produces global precipitation estimates from passive microwave and infrared data at high spatial and temporal resolution, *J. Hydrometeor.*, *5*(3), 487–503.
Kawanishi, T., T. Sezai, Y. Ito, K. Imaoka, T. Takeshima, Y. Ishido, A. Shibata, M. Miura, H. Inahata, and R. W. Spencer (2003), The Advanced Microwave Scanning Radiometer for the Earth Observing System (AMSR-E), NASDA's contribution to the EOS for global energy and water cycle studies, *IEEE Trans. Geosci. Remote Sens.*, *41*(2), 184–194.
Kida, S., S. Shige, T. Kubota, K. Aonashi, and K. Okamoto (2009), Improvement of rain/no-rain classification methods for microwave radiometer observations over the ocean using a 37 GHz emission signature, *J. Meteorol. Soc. Japan*, *87A*, 165–181.
Kozu, T., T. Kawanishi, H. Kuroiwa, M. Kojima, K. Oikawa, H. Kumagai, K. Okamoto, M. Okumura, H. Nakatsuka, and K. Oikawa (2001), Development of precipitation radar on board the Tropical Rainfall Measuring Mission satellite, *IEEE Trans. Geosci. Remote Sens.*, *39*(1), 102–116.
Kubota, T., et al. (2007), Global precipitation map using satellite-borne microwave radiometers by the GSMaP project: Production and validation, *IEEE Trans. Geosci. Remote Sens.*, *45*(7), 2259–2275.
Kubota, T., T. Ushio, S. Shige, S. Kida, M. Kachi, and K. Okamoto (2009), Verification of high resolution satellite-based rainfall estimates around japan using a gauge-calibrated ground radar dataset, *J. Meteorol. Soc. Japan*, *87A*, 203–222.
Kummerow, C., W. Barnes, T. Kozu, J. Shiue, and J. Simpson (1998), The Tropical Rainfall Measuring Mission (TRMM) sensor package, *J. Atmos. Ocean. Technol.*, *15*(3), 809–817.
Kummerow, C., Y. Hong, W. S. Olson, S. Yang, R. F. Adler, J. McCollum, R. Ferraro, G. Petty, D. B. Shin, and T. T. Wilheit (2001), The evolution of the Goddard profiling algorithm (GPROF) for rainfall estimation from passive microwave sensors, *J. Appl. Meteorol.*, *40*(11), 1801–1820.
Kunkee, D. B., G. A. Poe, D. J. Boucher, S. D. Swadley, Y. Hong, J. E. Wessel, and E. A. Uliana (2008), Design and evaluation of the first special sensor microwave imager/sounder, *IEEE Trans. Geosci. Remote Sens.*, *46*(4), 863–883.
Lau, K. M., and H. T. Wu (2003), Warm rain processes over tropical oceans and climate implications, *Geophys. Res. Lett.*, *30*(24), 2290, doi:10.1029/2003GL018567.
Liu, G. (1998), A fast and accurate model for microwave radiance calculations, *J. Meteorol. Soc. Japan*, *76*(2), 335–343.
Mo, T. (1996), Prelaunch calibration of the Advanced Microwave Sounding Unit-A for NOAA-K, *IEEE Trans. Microw. Theory Tech.*, *44*(8), 1460–1469.
Okamoto, K., and S. Shige (2008), TRMM precipitation radar and its observation results (in Japanese), *IEICE Trans. Commun. Japan*, *J91-B*, 723–733.
Olson, W. S., et al. (2006), Precipitation and latent heating distributions from satellite passive microwave radiometry. Part I: Improved method and uncertainty estimates, *J. Appl. Meteorol.*, *45*(5), 702–720.
Petty, G. (1994), Physical retrievals of over-ocean rain rate from multichannel microwave imagery. Part I: Theoretical characteristics of normalized polarization and scattering indices, *Meteorol. Atmos. Phys.*, *54*(1), 79–99.
Rosenfeld, D. E. A., and D. B. Wolff (1995), Improved accuracy of radar WPMM estimated rainfall upon application of objective classification criteria, *J. Appl. Meteor.*, *34*(1), 212–223.
Saunders, R. W., T. J. Hewison, S. J. Stringer, and N. C. Atkinson (1995), The radiometric characterization of AMSU-B, *IEEE Trans. Microw. Theory Tech.*, *43*(4), 760–771.
Schumacher, C., and R. A. Houze (2000), Comparison of radar data from the TRMM satellite and Kwajalein oceanic validation site, *J. Appl. Meteor.*, *39*(12), 2151–2164.
Shige, S., T. Watanabe, H. Sasaki, T. Kubota, S. Kida, and K. Okamoto (2008), Validation of western and eastern Pacific rainfall estimates from the TRMM PR using a radiative transfer model, *J. Geophys. Res.*, *113*, D15116, doi:10.1029/2007JD009002.
Shige, S., T. Yamamoto, T. Tsukiyama, S. Kida, H. Ashiwake, T. Kubota, S. Seto, K. Aonashi, and K. Okamoto (2009), The GSMaP precipitation retrieval algorithm for microwave sounders. Part I: Over-ocean algorithm, *IEEE Trans. Geosci. Remote Sens.*, *47*(9), 3084–3097.
Shimizu, S., R. Oki, T. Tagawa, T. Iguchi, and M. Hirose (2009), Evaluation of the effects of the orbit boost of the TRMM satellite on PR rain estimates, *J. Meteorol. Soc. Japan*, *87A*, 83–92.
Smith, E. A., et al. (2007), International global precipitation measurement (GPM) program and mission: an overview, in *Measuring Precipitation From Space-EURAINSAT and the Future*, edited by V. Levizzani, P. Bauer, and F. J. Turk, pp. 611–633, Springer, New York.
Stephens, G. L., and C. D. Kummerow (2007), The remote sensing of clouds and precipitation from space: A review, *J. Atmos. Sci.*, *64*(11), 3742–3765.
Surussavadee, C., and D. H. Staelin (2008a), Global millimeter-wave precipitation retrievals trained with a cloud-resolving numerical weather-prediction model. Part I: Retrieval design, *IEEE Trans. Geosci. Remote Sens.*, *46*(1), 99–108.
Surussavadee, C., and D. H. Staelin (2008b), Global millimeter-wave precipitation retrievals trained with a cloud-resolving numerical

weather-prediction model. Part II: Performance evaluation, *IEEE Trans. Geosci. Remote Sens.*, *46*(1), 109–118.

Takahashi, N., and T. Iguchi (2008), Characteristics of TRMM/PR system noise and their application to the rain detection algorithm, *IEEE Trans. Geosci. Remote Sens.*, *46*(6), 1697–1704.

Ushio, T., et al. (2009), A Kalman filter approach to the Global Satellite Mapping of Precipitation (GSMaP) from combined passive microwave and infrared radiometric data, *J. Meteorol. Soc. Japan*, *87A*, 137–151.

Vila, D., R. Ferraro, and R. Joyce (2007), Evaluation and improvement of AMSU precipitation retrievals, *J. Geophys. Res.*, *112*, D20119, doi:10.1029/2007JD008617.

Weng, F., and N. C. Grody (2000), Retrieval of ice cloud parameters using a microwave imaging radiometer, *J. Atmos. Sci.*, *57*(8), 1069–1081.

Wolff, D. B., D. A. Marks, E. Amitai, D. S. Silberstein, B. L. Fisher, A. Tokay, J. Wang, and J. L. Pippitt (2005), Ground validation for the Tropical Rainfall Measuring Mission (TRMM), *J. Atmos. Oceanic Technol.*, *22*(4), 365–380.

Zhao, L., and F. Weng (2002), Retrieval of ice cloud parameters using the Advanced Microwave Sounding Unit, *J. Appl. Meteorol.*, *41*(4), 384–395.

S. Kida and S. Shige, Graduate School of Science, Kyoto University, Kyoto, Japan. (satoshi.kida@kugi.kyoto-u.ac.jp; shige@kugi.kyoto-u.ac.jp)

T. Manabe, Department of Aerospace Engineering, Osaka Prefecture University, Sakai, Japan. (manabe@ieee.org)